An observational study of the response of the upper atmosphere of Mars to lower atmospheric dust storms

Paul Withers [a,*], R. Pratt [b]

[a] Astronomy Department, Boston University, 725 Commonwealth Avenue, Boston, MA 02215, USA
[b] Center for Space Physics, Boston University, 725 Commonwealth Avenue, Boston, MA 02215, USA

ABSTRACT

The effects of dust storms on densities, temperatures, and winds in the lower atmosphere of Mars are substantial. Here we use upper atmospheric observations to investigate how dust storms affect the upper atmosphere of Mars. We use aerobraking accelerometer, ultraviolet stellar occultation, and radio occultation datasets to examine the magnitudes and timescales associated with upper atmospheric density changes during dust storms. We find that: (1) Upper atmospheric conditions can be perturbed by dust storms outside the classical "dust storm season" of Ls = 180–360°. (2) The upper atmospheric regions affected by even a small dust event can include nearly all latitudes. (3) Atmospheric temperatures can be affected by dust storms at altitudes as high as 160 km. (4) The onset of the upper atmospheric response to a distant dust event can be a few days or less. (5) The characteristic timescale for the decay of the upper atmospheric response to a dust event can be 20–120° of Ls, and it may differ from the corresponding timescale for the lower atmosphere. (6) Average upper atmospheric densities can change by factors of a few during mere regional dust storms and an order of magnitude change is possible for the largest storms: these are general trends and individual density measurements may be greater than suggested by a general trend by a factor of two due to the intrinsic variability of the upper atmosphere. The decay timescale and magnitude of the upper atmospheric response depend on altitude, and larger events have shorter decay timescales. The substantial effects seen in the upper atmosphere illuminate the vertical extent of modified atmospheric circulation patterns and associated adiabatic heating/cooling during extreme dust loading, timescales for the onset and decay of the upper atmospheric response, and highlight potential dangers to spacecraft operations.

© 2013 Elsevier Inc. All rights reserved.

1. Introduction

Dust storms are the most dynamic events to disturb the atmosphere of Mars. During a dust storm, the amount of dust suspended in the atmosphere is significantly increased. Dust is not confined to the lowest few scale heights, but can extend well up into the mesosphere (Clancy et al., 2010). The effects of dust storms on lower atmospheric conditions have been studied extensively, with the topics that have been addressed by authors including dust storms' seasonal range, spatial coverage, disruption to circulation patterns, modification of tides, and effects on temperatures (e.g. Heavens et al., 2011a,b; Elteto and Toon, 2010; Cantor et al., 2010; Clancy et al., 2010; Hinson and Wang, 2010; Elteto, 2009; Rafkin, 2009; Smith, 2008; Cantor, 2007; Montabone et al., 2006; Withers and Smith, 2006; Gurwell et al., 2005; Montabone et al., 2005; Böttger et al., 2004; Smith et al., 2002). Changes in upper atmospheric conditions during dust storms have previously been reported for Mar-

iner 9 observations by Stewart and Hanson (1982) and Hantsch and Bauer (1990) and for Mars Global Surveyor (MGS) observations by Keating et al. (1998). The general behavior found was a sudden increase in density followed by a gradual decline.

Here we use a range of datasets to examine how dust storms impact the upper atmosphere. Since dust is not lofted into the upper atmosphere during a dust storm, numerical models predict that upper atmospheric density changes during dust storms are an indirect response to enhanced dust loading (Bougher et al., 1997, 1999; Bell et al., 2007). As dust is radiatively active, its presence and spatial distribution affect local atmospheric temperatures, which in turn affect atmospheric dynamics—even in regions where the dust content is not enhanced. Changes in the adiabatic heating caused by atmospheric circulation affect atmospheric densities. In addition, densities at all higher altitudes are affected by the raising of pressure levels below as the atmosphere expands outwards.

We aim to determine how quickly and by how much upper atmospheric densities change during the waxing and waning phases of dust storms. These observational findings can be used

to test the ability of numerical models to simulate accurately the chain of processes linking temporal, vertical, and horizontal trends in lower atmospheric dust content to temporal, vertical, and horizontal trends in upper atmospheric densities, thereby elucidating the atmospheric physics that control the thermal and dynamical state of the atmosphere of Mars.

Our investigation is of particular relevance for "whole atmosphere" studies that cross traditional boundaries between atmospheric regions (e.g., Heavens et al., 2011a; González-Galindo et al., 2009; McDunn et al., 2010; Kleinböhl et al., 2009). Studies of the upper atmospheric response to dust storms are also important for continued spacecraft exploration of Mars. Sudden, hard-to-predict changes in upper atmospheric densities (e.g., Keating et al., 1998; Withers et al., 2003; Withers, 2006; Fritts et al., 2006) are an operational challenge for an orbiter with a low periapsis altitude, such as MAVEN.

Contemporaneous dust opacity measurements are important for interpretation of the available upper atmospheric observations. Seasonal and interannual variations in atmospheric dust opacity are shown in Fig. 8 of Smith (2008) (MGS TES) and Fig. 6 of Smith (2009) (Odyssey THEMIS). These data show that infrared dust opacities greater than 0.2 are common at Ls = 180° to Ls = 360°. Indeed, in some years, such as Mars Years (MYs) 25 and 28, infrared dust opacities during these seasons exceeded 0.5 globally for months at a time. The timescale over which dust opacities increase significantly at the onset of these global-scale dust storms is very short, only a few days, and the thermal structure and dynamics of the atmosphere respond equally rapidly.

Section 2 describes the upper atmospheric and dust datasets used in this work; Section 3 reports our analysis of these datasets; Section 4 synthesizes our results; Section 5 interprets our results in the context of numerical simulations; and Section 6 summarizes our conclusions.

2. Available upper atmospheric data

We focus on three types of upper atmospheric measurements: (1) Aerobraking accelerometer observations of atmospheric densities; (2) radio occultation observations of the altitude of peak ionospheric electron density; and (3) ultraviolet stellar occultation measurements of vertical profiles of atmospheric density, pressure, and temperature.

Aerobraking accelerometer density measurements were obtained by MGS (Phase 1 and Phase 2), Mars Odyssey, and Mars Reconnaissance Orbiter (MRO) (Keating et al., 1998; Tolson et al., 1999, 2005, 2007; Withers et al., 2003; Withers, 2006). These orbiters made repeated passes through the atmosphere to adjust their orbital trajectories, with a typical periapsis altitude around 110 km. They measured along-track profiles of atmospheric density up to 160 km altitude, spanning several tens of degrees in latitude. Due to their near-polar, sun-synchronous orbits, an individual periapsis pass sampled a narrow range of longitudes and local times, except when periapsis was close to a pole. Orbital precession caused periapsis latitude to change secularly during aerobraking. The dates and locations sampled by these three missions were summarized by Tolson et al. (2005, 2007), Withers et al. (2003), and Withers (2006). In this work, we use densities archived at 10 km altitude intervals (e.g., 120 km, 130 km), not the time series density profiles themselves.

Here we use MGS Phase 1 accelerometer data. MGS Phase 2 and MRO accelerometer data were not acquired during dust storms. Odyssey data were acquired during a dust storm (Smith et al., 2002; Smith, 2004; Withers, 2006), but did not capture the pre-storm baseline. Also, since Odyssey's periapsis was traversing the north pole during the dust storm, densities were strongly affected

by changing latitude and local time. Given these complexities, we do not use these data here. However, comparison of Odyssey data and numerical simulations of atmospheric conditions during a dust storm would be illuminating.

Peak electron densities in the Mars ionosphere occur at a predictable pressure level of ~1 nbar times the cosine of the solar zenith angle (Withers, 2009). This is usually in the 120–150 km range. During a dust storm, enhanced heating causes the entire atmospheric column to expand, which raises the altitude of fixed pressure levels, even those above the altitudes experiencing heating. This increases the altitude of the pressure level of the ionospheric peak.

Vertical profiles of ionospheric electron densities have been measured by radio occultation instruments on many Mars orbiter missions, including Mariner 9, Viking Orbiter 1 and 2, MGS, and Mars Express (Hinson et al., 1999; Pätzold et al., 2004; Mendillo et al., 2006; Withers et al., 2008). Their vertical resolution is on the order of 1 km.

Here we use observations by Mariner 9 (standard mission), which operated during a particularly intense dust storm in its standard mission, and MGS, which collected many observations at a relatively fast and steady rate during a minor dust event.

The SPICAM UV spectrometer on Mars Express has produced several hundred vertical profiles of atmospheric density, pressure, and temperature from 70 to 120 km using the stellar occultation technique (Bertaux et al., 2004, 2006; Quémerais et al., 2006; Forget et al., 2009; McDunn et al., 2010; Withers et al., 2011). Their vertical resolution is on the order of 1 km. The dates and locations sampled by these measurements are shown in Fig. 1 of Forget et al. (2009).

3. Analysis of observations

In the following subsections, we present MGS accelerometer, Mariner 9 radio occultation, Mars Express SPICAM ultraviolet stellar occultation, and MGS radio occultation data. In many instances, we determine the increase in atmospheric density at dust storm onset and the timescale over which densities return to pre-storm values. Such timescales are often reported as "decay" timescales. Note that this terminology is formally associated with the response of a system to an impulsive or step function input, an idealized situation that does not apply here. Dust storms are a more complex perturbation and the density data are not acquired at fixed latitude, longitude, or local time. Nevertheless, this terminology is too familiar for us to replace it with more formally correct alternatives.

3.1. MGS accelerometer data

Phase 1 of MGS aerobraking commenced on 11 September 1997 (Ls = 179° of MY 23) and ended on 27 March 1998 (Ls = 301° of MY 23). Spacecraft operations were severely impacted by a strong regional dust storm that originated in Noachis Terra (40°S, 20°E) during aerobraking. Infrared dust opacities for this time period were reported by Christensen et al. (1998) and Smith et al. (2000). The dust opacity exceeded 0.7 over a wide swath of the southern hemisphere poleward of 40°S at the peak of the storm, with some measurements greater than 1.25. Smith et al. (2000) reported an exponential decay constant of 49 sols (32° of Ls) for the main Noachis storm at 45°S–60°S and 60°S–75°S, with longer timescales at more northern latitudes.

Upper atmospheric densities measured by the MGS accelerometer experiment show a strong response to this storm. Fig. 1 shows density as a function of season, Ls, during this storm for altitudes of 130, 140, 150, and 160 km on both inbound and outbound legs of
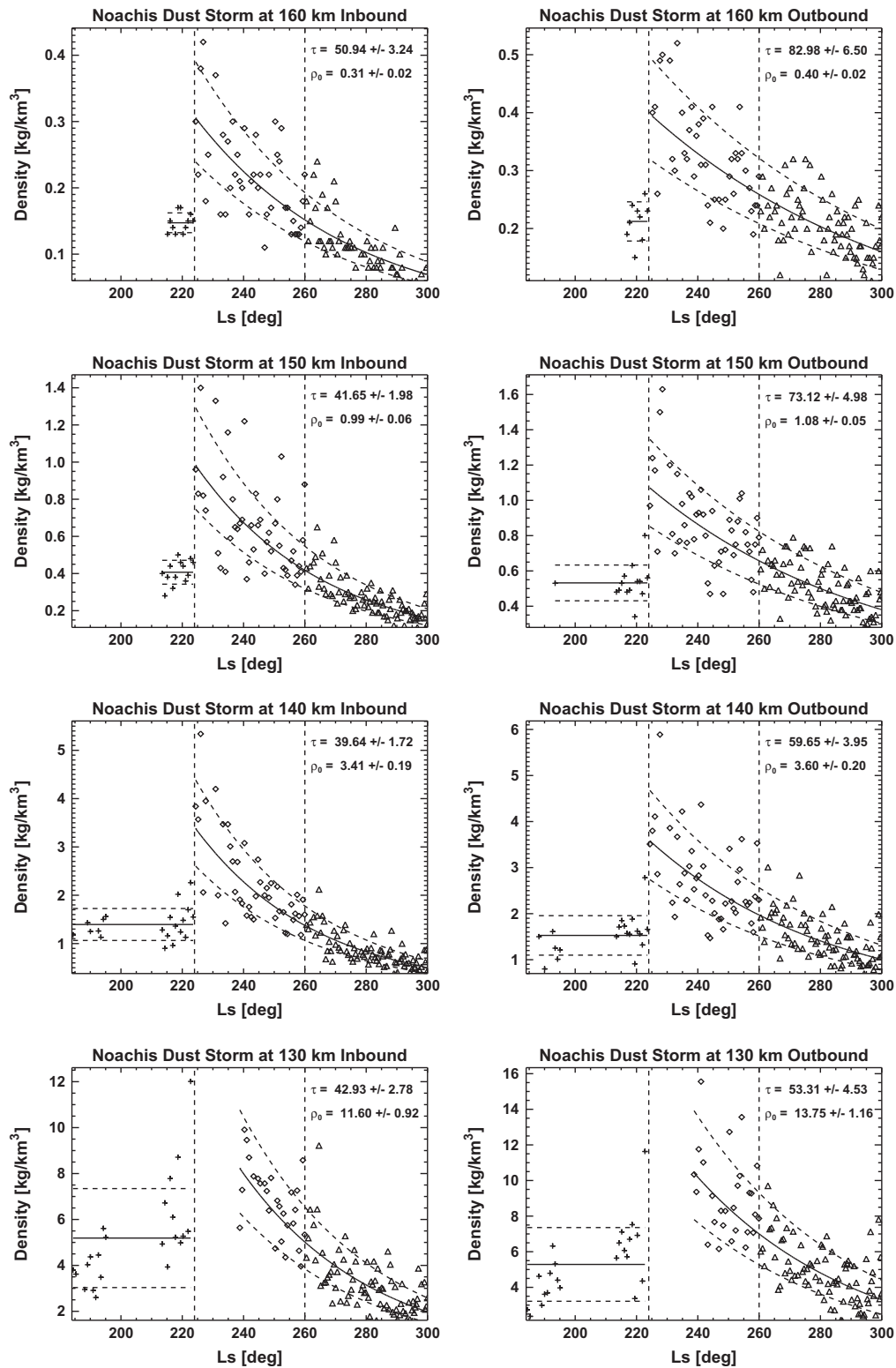
Fig. 1. Atmospheric densities measured by the MGS accelerometer during the Noachis dust storm. Individual panels correspond to different altitudes and either inbound or outbound legs of aerobraking passes. Inbound data are in the left column and outbound data in the right column. Data from 160 km are in the topmost row, and data from 150, 140, and 130 km are in the lower rows. In each panel, crosses indicate measurements obtained before Ls = 224°, the date of storm onset; diamonds indicate measurements between Ls = 224° and Ls = 260°; and triangles indicate measurements obtained after Ls = 260°. Ls = 260° is highlighted to represent the time when post-storm upper atmospheric conditions are similar to their pre-storm values. Vertical dashed lines mark the boundaries of these periods. The solid horizontal line shows the mean pre-storm density and the dashed horizontal lines show the 1-σ standard deviation about this mean. The curved solid line shows the best-fit exponential curve to densities measured between Ls = 224° and 300°, and the flanking dashed lines show 1-σ confidence intervals about this fit. τ is the fitted decay timescale in units of degrees of Ls and ρ_0 is the fitted peak density in units of kg km^{-3}.

Table 1

Atmospheric densities measured by the MGS accelerometer during the Noachis dust storm and related properties. The latitude range reported for each set of measurements corresponds to Ls = 224° to Ls = 260°. ρ_0 is the fitted density at the peak of the storm, ρ_{pre} is the average pre-storm density, r is ρ_0/ρ_{pre}, τ_{fit} is the decay timescale obtained by a direct exponential fit to the data, τ_s is the background decay timescale associated with changes in season and latitude, and τ_{cor} is the corrected decay timescale. All uncertainties are 1σ.

Altitude (km)	Direction	Latitude (°N)	ρ_0 (kg km^{-3})	ρ_{pre} (kg km^{-3})	r (–)	τ_{fit} (°)	τ_s (°)	τ_{cor} (°)
130	Inbound	43.1–51.8	11.60 ± 0.92	5.19 ± 2.16	2.24 ± 0.95	42.93 ± 2.78	80	93 ± 3
130	Outbound	32.6–39.1	13.75 ± 1.16	5.29 ± 2.07	2.60 ± 1.04	53.31 ± 4.53	160	80 ± 5
140	Inbound	44.2–54.5	3.41 ± 0.19	1.39 ± 0.33	2.45 ± 0.60	39.64 ± 1.72	90	71 ± 2
140	Outbound	32.2–36.4	3.60 ± 0.20	1.53 ± 0.43	2.36 ± 0.67	59.65 ± 3.95	187	87 ± 4
150	Inbound	46.9–56.5	0.99 ± 0.06	0.41 ± 0.06	2.44 ± 0.41	41.65 ± 1.98	76	93 ± 2
150	Outbound	29.5–34.4	1.08 ± 0.05	0.53 ± 0.10	2.02 ± 0.40	73.12 ± 4.98	234	106 ± 5
160	Inbound	49.0–58.3	0.31 ± 0.02	0.15 ± 0.01	2.08 ± 0.25	50.94 ± 3.24	100	104 ± 3
160	Outbound	27.5–32.6	0.40 ± 0.02	0.21 ± 0.03	1.88 ± 0.31	82.98 ± 6.50	279	118 ± 7

the aerobraking passes. Sudden, substantial, and persistent density increases occur around Ls = 224° at all altitude levels. These measurements at Ls = 224° were made at 35°N to 60°N and local times of 10–18 h.

The average pre-storm density, ρ_{pre}, was calculated for each set of data in Fig. 1. In addition, an exponential decay curve was fitted to each set of data so that the fitted density at dust storm onset, ρ_0, and decay timescale, τ_{fit}, could be calculated. The ratio r of peak to pre-storm density was also calculated. Results and other information are listed in Table 1.

However, the fitted decay timescales should not be interpreted literally. For all panels in Fig. 1, the post-storm density falls below the pre-storm density. Atmospheric conditions are not settling back to the pre-storm state, they are instead overshooting. The measurements move northward towards the winter pole during this period, which will cause densities to decrease. In addition, the season advances into winter, which will also cause densities to decrease. Hence the fitted decay timescales combine the effects of the waning dust storm, the changing latitude, and the changing season.

A corrected decay timescale provides a better characterization of the effects of the waning dust storm. Suppose that the dust storm effects are associated with a decay rate λ_d and the meridional and seasonal effects are associated with a decay rate λ_s. The fitted timescale τ_{fit} satisfies $1/\tau_{fit} = \lambda_d + \lambda_s$. The decay rate λ_s can be obtained by comparing the pre-storm densities at Ls = 224° and final densities at Ls = 300°. For example, consider inbound data at 160 km where the pre-storm density was 0.15 kg km^{-3} and the final density was 0.07 kg km^{-3}. The corresponding decay rate λ_s is 100 deg^{-1}. For a fitted timescale τ_{fit} of 50.94 ± 3.24°, the corrected timescale for the decay of the dust storm effects is 104 ± 3°. Corrected decay timescales, which are on the order of 100° of Ls, are listed in Table 1.

Densities at upper atmospheric altitudes doubled in this storm. Note that this density doubling occurred from one orbit to the next, in at most 0.8° of Ls. The onset of elevated densities occurred at the same time, orbit 53 (Ls = 224.4°), in all altitude levels. Densities were normal on orbit 52 (Ls = 223.6°), 30 h earlier. By contrast, elevated dust opacities were first detected in the lower atmosphere on orbit 50 (Ls = 221.9°), a few days earlier, in the southern hemisphere. Smith et al. (2000) reported the first increases in northern hemispheric dust opacities on orbit 53, the orbit on which these upper atmospheric density changes began. However, it is possible that unobserved changes occurred in the northern hemisphere earlier. Indeed, Plate 3 of Smith et al. (2000) suggests an increase in northern hemispheric dust opacities near longitude 0°E on orbit 50, 3–4 sols prior to orbit 53, although no such increase was observed in northern hemispheric observations at other longitudes on orbits 51 and 52. Does the three orbit gap between the first detection of the dust storm and the first detection of an upper atmospheric response imply that changes in atmospheric circula-

tion and associated adiabatic heating in the northern hemisphere occurred immediately in response to changes in dust conditions in the northern hemisphere? Or does it imply that these changes occurred belatedly in response to large changes in dust conditions in the southern hemisphere? Useful perspective on this issue is provided by the assimilation of MGS TES temperature and dust data into a general circulation model by Lewis et al. (2007). They found that "there is a growth of 50% in the peak strength of the mean circulation over the course of a few sols" at the onset of the Noachis storm. They also emphasized that "the meridional circulation becomes much more unsteady" during the storm and can double in strength over about one sol. However, they did not examine their global density results on the sol-by-sol timescale over which aerobraking data were collected.

It is noteworthy that the upper atmospheric response occurred at all observed locations simultaneously. These data span latitudes of 35°N to 60°N, whereas the storm originated at 40°S, showing that the upper atmospheric impact of a dust storm, although it may lag the onset of the storm, can advance over 25° of latitude in a time period of less than 0.8° of Ls.

For the outbound data, the density enhancement factor decreases monotonically from 2.6 to 1.9 with either decreasing latitude or increasing altitude *and* the corrected decay timescales increases in the same manner from 80° to 118°. Indeed, the products of these corrected decay timescale and their corresponding density enhancement factors are much closer together (205–222°, a range of only ±4% about the mean). If this is not just a coincidence, it would suggest that larger density enhancements decay more quickly than small ones. These trends are not present in the more poleward inbound data, although there is a hint that the corrected decay timescale increases with either increasing latitude or increasing altitude, which would favor altitude as the more likely controlling factor. An exploration of these trends with numerical simulations would be valuable, particularly for identifying whether latitude or altitude is the key factor in the observed behaviors. Since 1° of Ls equals about 1.5 sols at this season, our fitted decay timescales of 70–120° (about 105–180 sols) are broadly consistent with the "longer than 49 sols" timescale found by Smith et al. (2000).

Atmospheric densities may have increased at 130–160 km during this storm, but the highest altitude at which temperatures were increased is less clear. In an earlier study of this dataset, Keating et al. (1998) found a greater density enhancement at a reference altitude of 126 km than 61 km, which they suggested was due to additional warming in the 70–120 km region (a region for which direct observations were not available). That is, this dust storm increased atmospheric temperatures up to altitudes of at least 70 km.

This storm has challenged numerical models: Bougher et al. (1999) simulated these upper atmospheric conditions using simplified dust conditions and found that upper atmospheric densities
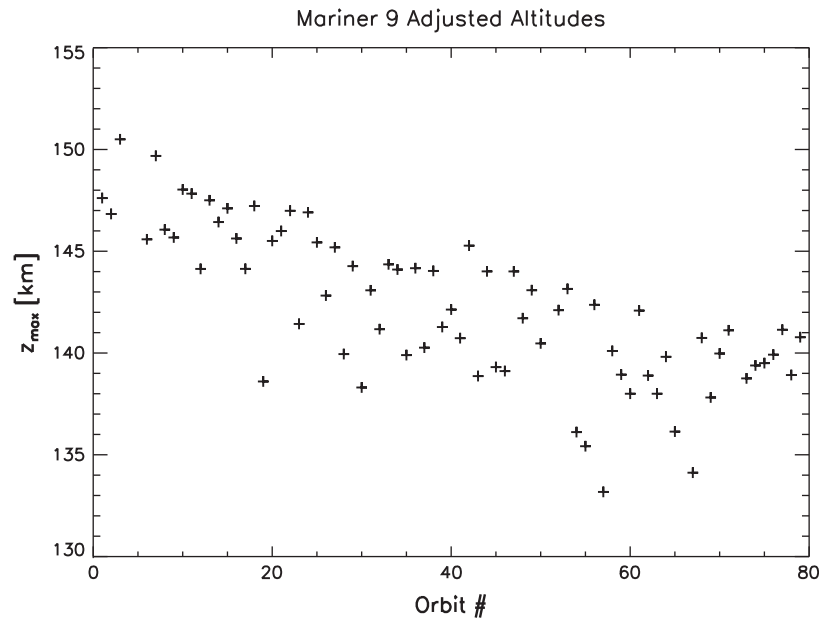
Mariner 9 Adjusted Altitudes

Fig. 2. Adjusted ionospheric peak altitudes from the standard mission of Mariner 9, reported relative to the MOLA areoid.

were under-predicted by a factor of three for simulations with static visible dust opacities of 0.3 and 1.0.

3.2. Mariner 9 radio occultation data

The Mariner 9 mission arrived at Mars during the decay of perhaps the largest dust storm ever recorded (Smith et al., 2000). Ionospheric peak altitudes observed during the Mariner 9 standard mission (Fig. 2) were 20–30 km higher than normal (Fig. 3 of Hantsch and Bauer (1990)), and this altitude offset has long been attributed to expansion of the atmosphere due to this dust storm. Also, the peak altitudes dropped steadily with time in parallel with the waning of the dust storm. McElroy et al. (1977) found that the effective temperature of the atmosphere below the ionospheric peak had to be 20 K warmer than usual to account for the increased peak altitude, and Kliore et al. (1973) found that the atmosphere below the ionospheric peak had to cool by 25–30% (more than the 20 K of McElroy et al. (1977)) after the standard mission. Wang and Nielsen (2003) used an ionospheric model to infer that the neutral density at 100 km decreased by a factor of two over the standard phase of the Mariner 9 mission.

Kliore et al. (1972) listed ionospheric peak altitudes for the standard mission occultations, but these were based on the Mars areoid as understood in the Mariner 9 era. Substantial improvements in Mars geodesy have occurred since then, especially the acquisition of complete and accurate maps of the areoid and topography by the MOLA instrument on MGS (Smith et al., 2001). Accordingly, we used the peak radii, latitudes, and longitudes reported by Kliore et al. (1972) to find peak altitudes relative to the MOLA areoid. These are shown in Fig. 2 and we use these adjusted peak altitudes in the remainder of this work. We have not located a list of the times of these occultations, but they can be calculated knowing that the Mariner 9 orbital period was 12 h (chosen partially for reasons of operational simplicity) and orbit insertion occurred on 14 November 1971.

After adjustment, these peak altitudes are still much higher than usual. Hantsch and Bauer (1990) surveyed an extensive range of ionospheric measurements and found that typical peak altitudes could be represented as 120 km + 10 km × ln(sec SZA), where SZA is solar zenith angle. The solar zenith angles covered

by these Mariner 9 occultations are 47–56°, angles usually associated with a peak altitude of 126 km or less. The adjusted peak altitudes still drop dramatically with time, and this change is much greater than the 2 km shift contributed by changing solar zenith angle.

In order to make direct comparisons with the other sections of this paper, we do not analyze peak altitudes directly. Instead, we calculate implied changes in pressure at a fixed altitude level. If upper atmospheric pressure depends exponentially on altitude with scale height H and a dust storm causes pressure levels to shift rapidly upwards, then slowly back downwards, then the temporal evolution of the pressure at some fixed altitude level can be estimated from the changes in peak altitude. The ratio of the pressure at some fixed altitude in the upper atmosphere when the ionospheric peak altitude is z_{obs} to its value when the ionospheric peak altitude is z_{ref} is $\exp((z_{obs} - z_{ref})/H)$.

The inferred changes in pressure at fixed altitude level are sensitive to the choice of H. We adopt $H = 10$ km as our nominal value based upon the results of Hantsch and Bauer (1990) and Withers (2006). We also conducted a sensitivity study using $H = 8$ km and 12 km. We chose 138 km as z_{ref}, which corresponds to the peak altitude at the end of the series of occultations observed during the Mariner 9 standard mission (orbit 79). Note that the ionospheric peak on orbit 79 is still 10 km higher than it normally is, showing that the dust storm's effects have not fully abated (Hantsch and Bauer, 1990).

A pressure ratio, or relative pressure, of 1 corresponds to a peak altitude of 138 km, a relative pressure greater than 1 corresponds to a peak altitude above 138 km, and a relative pressure less than 1 corresponds to a peak altitude below 138 km. The relative pressures obtained by this procedure with $H = 10$ km are shown in Fig. 3. Here the relative pressures are shown as a function of Ls, not orbit number, for consistency with the rest of this paper. This shows that the relative pressure decreases with time, as expected for the waning phase of a dust storm. The decrease is well-represented by an exponential decay, which is shown by the fit in Fig. 3. The timescale for decay is 20° of Ls. If we instead use $H = 8$ km or 12 km, then the timescale becomes 16° or 24°, respectively. Fig. 3 shows that, if assuming $H = 10$ km, the pressure at a fixed altitude level was 2.7 times greater at the start of the

Mariner 9 Dust Storm

$\tau = 19.74 +/- 3.02$

$p_o = 2.71 +/- 0.19$
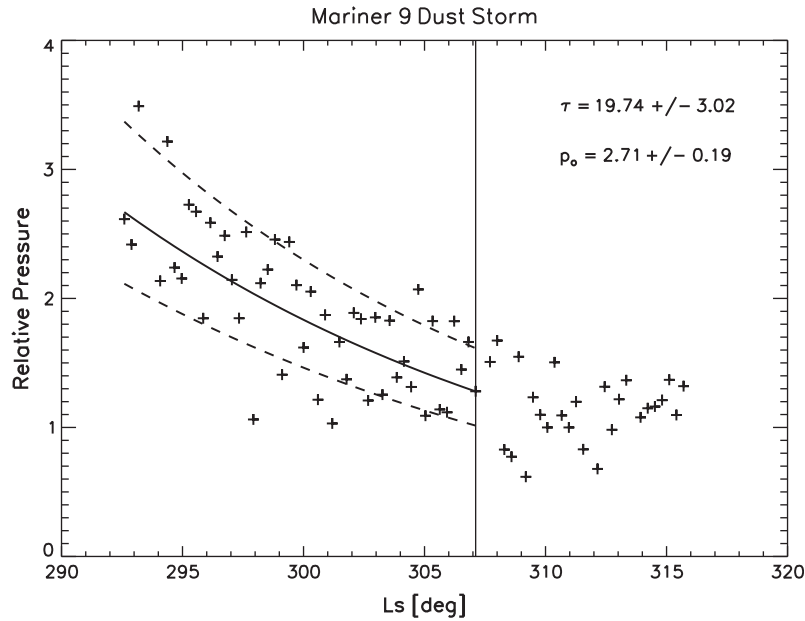
Fig. 3. Changes in atmospheric pressure at a fixed altitude relative to a benchmark that occurred during the Mariner 9 standard mission. These values were calculated as $\exp((z - z_o)/H)$, where z_o is 138 km, H is 10 km, and the peak altitudes z are Mariner 9 adjusted ionospheric peak altitudes. The curved solid line shows an exponential fit to data collected before orbit 50 (marked by the vertical line at Ls = 307°) and the flanking dashed lines show 1-σ confidence intervals about this fit. The fitted relative pressure at orbit insertion, p_o, which is dimensionless, and the fitted decay timescale, τ, which is given in units of degrees of Ls, are reported on the panel with 1-σ uncertainties.

standard mission than at orbit 79. If we instead use $H = 8$ km or 12 km, then this result becomes 3.5 or 2.3, respectively.

Stewart and Hanson (1982) reported a decay constant of 60 days (about 36° of Ls) for the dust storm's contribution to the difference between the observed ionospheric peak altitude and its normal value, significantly longer than that reported here. Their analysis has the ionospheric peak dropping by 12 km × (exp(0) − exp(−1)), or 7.6 km, over 60 days (about 36° of Ls) and 4.7 km over 30 days (about 18° of Ls). This underestimates the ∼10 km drop shown in Fig. 2 over 60 orbits by a factor of two. However, Stewart and Hanson (1982) did also include a dependence on heliocentric distance and solar zenith angle in their expression for peak altitude. Changes in solar zenith angle in their analysis can account for 2.8 km decrease in peak altitude by orbit 60 and remaining differences are consistent with the altitude corrections we have made.

The Mariner 9 investigators also determined decay timescales for lower atmospheric properties. Atmospheric optical thicknesses were acquired at ultraviolet wavelengths by Mariner 9 (Pang and Hord, 1973), but not at the visible and infrared wavelengths familiar from recent Mars missions, and atmospheric temperatures were measured at the 0.3 mbar and 2 mbar pressure levels (Conrath, 1975). Conrath (1975) used these data to conclude that the dust optical depth, decayed with an e-folding time of 60 days (about 36° of Ls). Analysis of the extinction of ultraviolet radiation by the atmosphere during the standard phase of the Mariner 9 mission (Pang and Hord, 1973) also suggested a 60 day settling time for atmospheric dust, although these authors found a linear, rather than exponential, decline in dust content.

Since the dust storm had not completely subsided by orbit 79, the pressures and densities at a fixed upper atmospheric altitude level at the start of the standard mission were more than 2.7 times greater than usual. The highest peak altitude in this dataset, 150 km, is about 25 km, or 2.5 scale heights, higher than the typical value of 125 km, which implies that upper atmospheric densities were 12 times greater than usual at the time of Mariner 9's arrival at Mars. Even larger densities likely occurred at earlier times during this remarkable storm.

3.3. Mars Express SPICAM ultraviolet stellar occultation data

Available SPICAM profiles span all seasons of MY 27. Forget et al. (2009) reported that SPICAM density measurements from 70 km to 130 km increased suddenly at Ls = 135°, outside the usual season for dust storms. The Odyssey THEMIS instrument measured dust opacities over this period (Smith, 2009). As shown in Fig. 4 (and also Fig. 6 of Smith (2009)), a relatively weak dust event occurred at this time. Fig. 5 shows the average dust opacity between 30°S and 30°N as a function of season using five degree wide Ls bins, confirming that tropical dust opacity increased at Ls = 135°. There are insufficient THEMIS data points to permit high time resolution analysis, but landed data from Spirit and Opportunity data are suitable, albeit limited in their geographic coverage. As shown in Fig. 6, a significant and sudden increase in dust opacity was also observed at the locations of Spirit and Opportunity at this time. This dust event is the simplest and most likely explanation for the observed sudden increase in upper atmospheric densities.

Dust opacities in excess of 0.2 are most common at Ls = 180° to Ls = 360°, but this half of the Mars Year is not the only period when
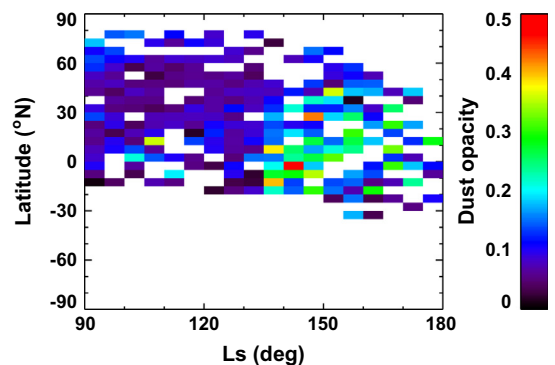
Fig. 4. THEMIS dust opacity (Smith, 2009) from MY 27 (data provided by Luca Montabone).
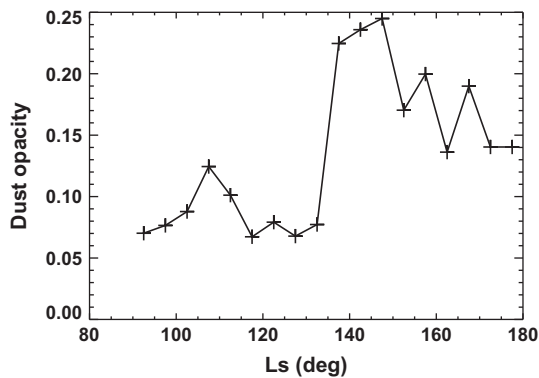
Fig. 5. Average tropical THEMIS dust opacity (Smith, 2009) at Ls = 90–180° from MY 27. Averages were calculated using all data equatorward of 30° latitude and 5° wide Ls bins (data provided by Luca Montabone).
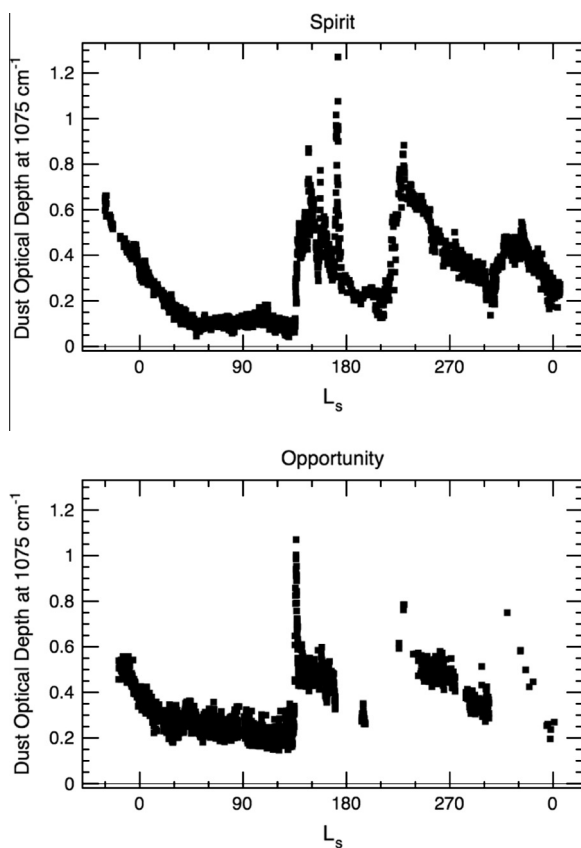

Fig. 6. Seasonal variations in dust opacity in MY 27 at the landing sites of Spirit (top) and Opportunity (bottom). Fig. 13 of Smith et al. (2006), reproduced by permission of the American Geophysical Union.

dust events may occur. Several apparently small dust events occur around Ls = 130° in the THEMIS dataset in MY 27, 28, and 29 (Smith, 2009). Although small from an orbital perspective, landed measurements by Spirit and Opportunity in MY 27 show that they may be comparable in magnitude, at least locally, to dust events at classical dust storm seasons.

Fig. 7 shows the affected SPICAM density measurements at altitudes from 60 km to 120 km. Densities in the pre-event interval of Ls = 115–125° are representative of those at earlier seasons and densities in the post-event interval of Ls = 135–145° degrees are representative of those at later seasons. During the intervening interval of 10° of Ls (20 days duration), densities increase substan-

tially. Our attempts to fit a useful functional form to the increase in density with Ls did not yield successful results. We calculated the density enhancement factor associated with this small dust event as the ratio of the post-event density to pre-event density and results are shown in Fig. 8. A similar analysis was conducted with SPICAM pressure measurements; it yielded similar results. The density and pressure enhancement factors are 2 at 60–80 km. There are suggestions, albeit without great statistical significance, that these enhancement factors increase with altitude from 60 km to 120 km. However, given that all eight density and pressure enhancement factors at 90–120 km exceed 3, the odds are small that there is no dependence on altitude for these enhancement factors.

A vertically-uniform density enhancement factor over a particular altitude range implies that temperatures in the altitude range are unaltered while all the heating responsible for atmospheric expansion is confined to lower altitudes. The apparent increase in density enhancement factor from 60 km to 120 km in SPICAM data implies that this particular dust event increased atmospheric temperatures at altitudes as high as 100 km. This can be compared to the apparent decrease in density enhancement factor from 130 km to 160 km in MGS accelerometer data (Section 3.1). If it is reasonable to analyze these two different datasets and two different dust storms together, then these observations imply atmospheric heating in the 60–120 km range and cooling in the 130–160 km range.

The timescales associated with atmospheric changes during this dust event are unusual. The onset of density changes is gradual, not sudden, and we have not localized it any better than to within a 10° wide Ls window. Also, the dust opacities observed by THEMIS, Spirit, and Opportunity dropped from their peak values over the next few tens of degrees of Ls, but no corresponding decrease in atmospheric densities at any altitude is readily discernable, which is unlike the behavior seen in upper atmospheric densities during the Noachis dust storm that disrupted MGS aerobraking in MY 23. This may be explained by a shift in the latitudes observed by SPICAM at about Ls = 170°, which can be seen in Fig. 7.

3.4. MGS radio occultation data

Due to a quirk of its orbital characteristics, MGS radio occultation observations of the ionospheric peak altitude, which is sensitive to dust storms, generally occurred outside dust storm seasons (Withers et al., 2008). Nevertheless, peak altitude data were acquired between Ls = 180° and Ls = 360° in two Mars Years. Measurements were acquired between Ls = 180° and Ls = 214° in MY 26, but dust opacities in this year were not yet elevated above background values at these seasons (Smith, 2008). Measurements were also acquired from Ls = 119° to Ls = 227° in MY 27, a year of relatively little dust activity (Smith, 2009). However, this period encompasses the dust event observed by SPICAM at Ls = 130° (Section 3.3). Fig. 9 shows that these measurements, acquired at 62.4°N to 80.1°N, are also affected by this dust event. Prior to the dust event, at Ls = 120 ± 1°, the ionospheric peak altitude was 135.2 ± 3.6 km. It reached a maximum of 140.0 ± 3.0 km at Ls = 138°, and decreased to 137.5 ± 2.2 km by Ls = 178°. Although the statistical significance of this increase in peak altitude is not great, a robust confirmation of a change in peak altitude around Ls = 130° can be produced by more aggressive seasonal averaging. Given these uncertainties, we have not fitted a timescale for the return of elevated peak altitudes to normal. However, one can be crudely estimated by noting that the peak altitude changes from 140.0 km at Ls = 138° to 137.2 km at Ls = 160° and applying the relative pressure methods of Section 3.2. This leads to a highly uncertain result of 80° of Ls.
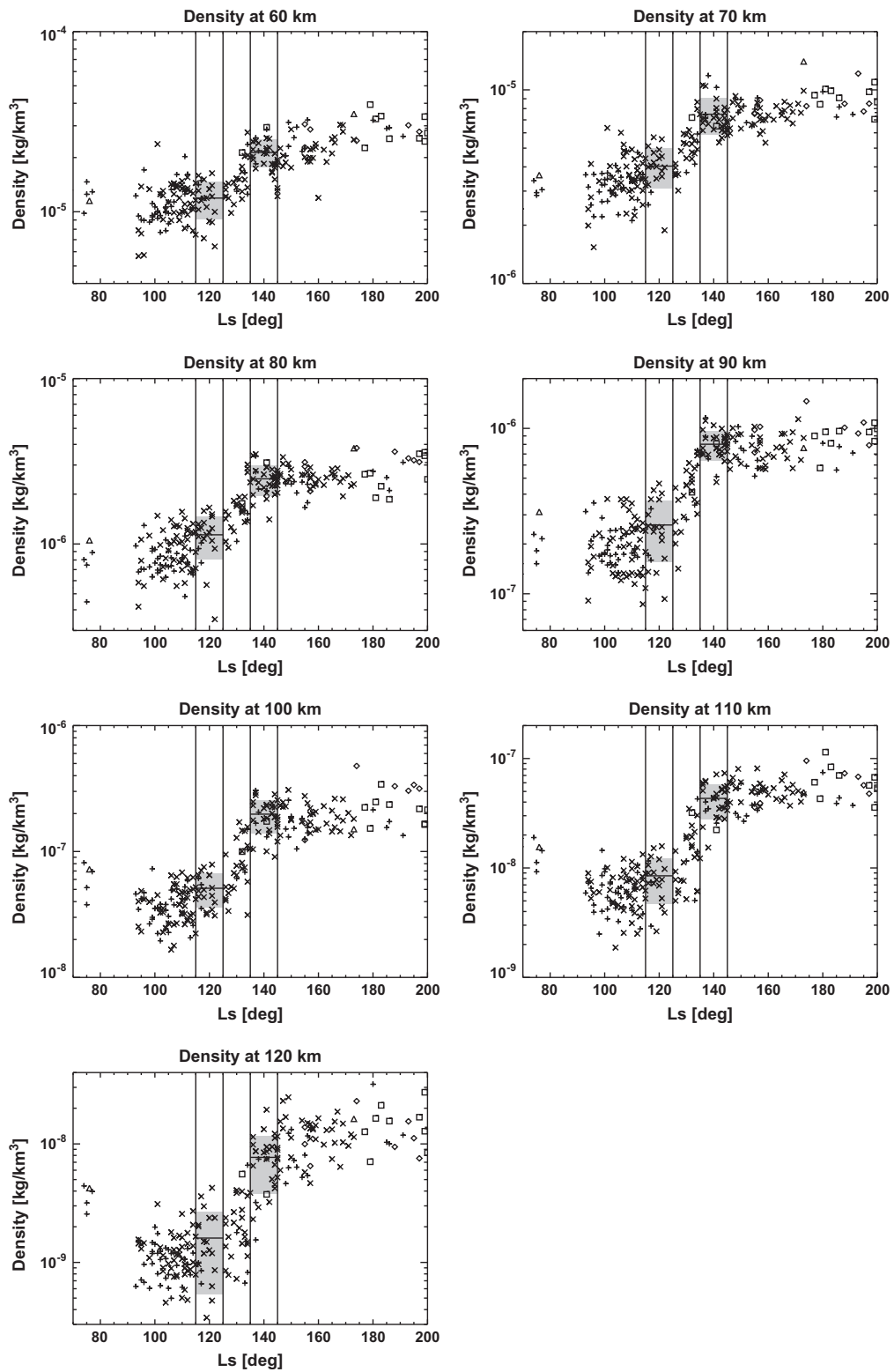
Fig. 7. Atmospheric densities measured by the SPICAM instrument at various altitudes between 50°N and 50°S. The top row shows data at 60 km (left) and 70 km (right). The next rows show 80 km and 90 km, 100 km and 110 km, and finally 120 km on the bottom row. In each panel, data are indicated by symbols that indicate latitude: × for 50°S–30°S, + for 30°S–10°S, triangles for 10°S–10°N, squares for 10°N–30°N, and diamonds for 30°N–50°N. Vertical lines identify a pre-event interval at Ls = 115–125° and a post-event interval at Ls = 135–145°. The two solid horizontal lines are the mean densities in each interval and the flanking shaded regions show the 1-σ standard deviation about these means.
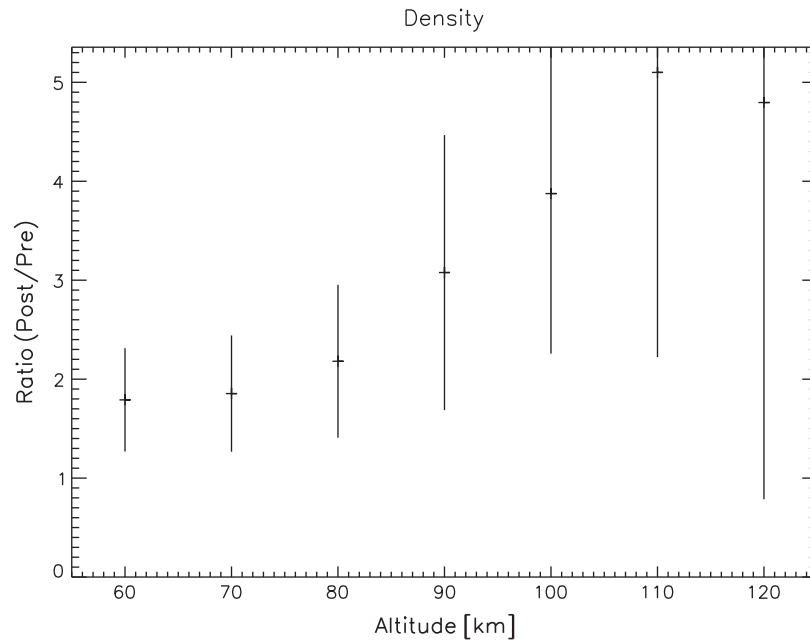
Fig. 8. Dependence on altitude of changes in SPICAM density measurements from Ls = 115–125° to Ls = 135–145° (Fig. 7). Crosses show the ratios of post-event densities to pre-event densities with the vertical extent of each cross indicating the 1-σ standard deviation.
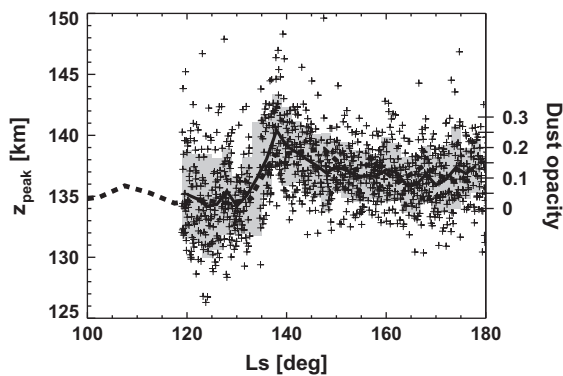
Fig. 9. Ionospheric peak altitudes measured at latitudes 62.4°N to 80.1°N by the MGS radio occultation instrument during the dust storm that perturbed SPICAM density and pressure measurements at Ls = 130° in MY 27. Data are shown as crosses. Mean altitudes for 2° wide Ls bins are shown by the thick solid line. The standard deviation in the peak altitude for each of these bins is shown by shaded gray boxes. The dashed line shows the average tropical dust opacity from Fig. 5.

At these altitudes, the SPICAM data suggest an increase in atmospheric density at fixed altitude of at least exp(1). This would correspond to an increase in peak altitude of one scale height, whereas the MGS radio occultation observations show a noticeably smaller increase, albeit with substantial uncertainties. The upper atmospheric response to this dust event was greater at 50°S–50°N (SPICAM data) than 62.4°N to 80.1°N (MGS data).

Fig. 9 also shows the average tropical dust opacity from Fig. 5. The correspondence between the tropical dust opacity (equatorward of 30° latitude) and the ionospheric peak altitude (poleward of 60°N) is striking These data do not have adequate time resolution to address the question of how rapidly the upper atmosphere responds to a distant dust event.

Fig. 4 shows that there is little dust loading in the atmosphere north of 40°N. Hence the upper atmosphere can be affected by distant dust events even when there is no dust activity in the lower atmosphere directly below.

4. Synthesis of results

Lower atmospheric dust storms have significant effects on upper atmospheric densities, even at distant latitudes, over a wide range of seasons. These effects arrive rapidly after storm onset and decay slowly.

4.1. Seasonal preferences

Sudden increases in upper atmospheric densities associated with lower atmospheric dust storms are not restricted to classical "dust storm season". TES and THEMIS orbital observations show that enhanced dust loading frequently occurs between Ls = 180° and Ls = 360°, but Spirit and Opportunity landed observations reveal a significant dust event at Ls = 135° in MY 27 that affected upper atmospheric densities measured by SPICAM and ionospheric peak altitudes measured by Mars Global Surveyor. In fact, this event can also be discerned in THEMIS orbital data, and similar dust events occurred at this season in MY 28 and 29 as well.

4.2. Latitudes at which upper atmospheric densities are affected

The upper atmospheric effects of dust storms can be global, not merely localized to regions where significant dust loading is present in the lower atmosphere. This is best illustrated by the Noachis dust storm during MGS Phase 1 aerobraking when a dust storm centered on 40°S affected upper atmospheric densities 6000 km away at 60°N. It is also shown by the changes in ionospheric peak altitude at high northern latitudes in MY 27 that coincided with THEMIS observations of a small dust event confined to tropical latitudes. However, the effects are not the same at all latitudes. The Ls = 135° event in MY 27 observed in the lower atmosphere by Spirit and Opportunity had a greater effect on SPICAM observations of the tropical and mid-latitude upper atmosphere than on Mars Global Surveyor observations of the upper atmosphere at 62.4°N to 80.1°N.

4.3. Altitudes at which temperatures are affected

Heating of the lower atmosphere affects densities at all higher altitudes, but what is the highest altitude that is directly heated? Heating associated with dust storms extends at least to the mesopause. SPICAM observations demonstrate that heating occurs in the 70–120 km range, consistent with the finding of Keating et al. (1998) that heating was present in the 70–120 km region during the Noachis dust storm. The apparent decrease in density enhancement factor from 130 km to 160 km in MGS accelerometer data implies cooling at these altitudes.

4.4. Timeliness of upper atmospheric response to dust storm onset

The interval between the first detectable dust storm precursors in the lower atmosphere and major changes in upper atmospheric density may be short. During Phase 1 of MGS aerobraking, the onset of the Noachis dust storm at 40°S preceded upper atmospheric impacts at 35°N to 60°N by only a few days. The onset of substantial upper atmospheric changes at 60°N were separated from the onset at 35°N by no more than 30 h. The transition from normal upper atmospheric densities to the peak values encountered during this storm occurred within 30 h, implying a sudden, rather than gradual, increase in densities.

4.5. Decay timescale for upper atmospheric changes

The timescale for the decay in upper atmospheric densities after the peak of a dust storm varies from case to case and is not identical to the decay timescale of the lower atmospheric dust content. For the MGS accelerometer observations, timescales of 70–120° of Ls were found. This is longer than the corresponding dust opacity decay timescales. For the Mariner 9 observations, a timescale of 20° of Ls was found, whilst lower atmospheric dust and temperature measurements during the Mariner 9 dust storm were characterized by a longer decay timescale of 36° of Ls. For the SPICAM observations, no decay was apparent at all, which may reflect observational biases. For the MGS RS observations, a timescale of 80° of Ls was roughly estimated. The nominal value of this uncertain result is longer than the dust opacity decay timescale inferred from Fig. 5.

The decay timescales found for the MGS accelerometer observations appear to increase with increasing altitude from 130 km to 160 km, and larger density enhancements decay more quickly than small ones. The physical explanation for these disparate results is not known. Numerical simulations that address relationships between dust storm decay timescale and strength and upper atmospheric decay timescale, altitude, and latitude would be valuable here.

4.6. Magnitude of upper atmospheric changes

The maximum enhancement in upper atmospheric density at fixed altitude during a dust storm also varies from case to case. For the MGS accelerometer observations, enhancement factors of 1.9–2.6 were found. For the Mariner 9 observations, an enhancement factor of 2.7 was found from orbits 1–79, although this used the still-elevated densities at orbit 79 of the standard mission as a reference. Indeed, an enhancement factor of 12 was implied by the difference between the first observations and normal conditions, and the peak of the storm preceded the first observations, implying an even greater enhancement factor at the peak of the storm. For the SPICAM observations, upper atmospheric densities at 110–120 km were enhanced by an uncertain factor whose most probable value is 5 and those at 60–70 km by an uncertain factor of 2. For

the MGS RS observations, an enhancement factor of 1.6 was roughly estimated.

Increases in upper atmospheric density by a factor of a few must be considered a commonplace response to moderate regional storms and an order of magnitude increase can occur in the largest storms. It should also be recognized that these results describe the average behavior of any available dataset. Individual measurements within a dataset may deviate substantially from this trend. Consider the 140 km outbound densities from Phase 1 of MGS aerobraking that are shown in Fig. 1. The mean pre-storm density is 1.5 kg km^{-3} and the maximum density suggested by the best-fit curve is 3.6 kg km^{-3}. One density measurement shortly after the onset of the storm's effects at upper atmospheric altitudes was almost 6 kg km^{-3}, six times the smallest density measured shortly before the storm's onset, four times the pre-storm mean, and almost two times the fitted maximum density.

The enhancement factor also seems to be influenced by altitude and latitude. It increases with altitude from 60 km to 120 km in SPICAM data, then decreases with altitude from 130 km to 160 km in MGS accelerometer data. It is smaller for the MGS RS observations at high northern latitudes than for SPICAM observations at the tropical and mid-latitudes that experienced significant enhancements in atmospheric dust content.

5. Numerical simulations and physical interpretations

The observed upper atmospheric phenomena summarized in Section 4 can be interpreted in terms of the atmospheric physics that are responsible with the aid of numerical simulations that connect observables to processes. We first summarize key studies applying numerical simulations to the upper atmospheric effects of dust storms.

Bougher et al. (1997) reported some of the first general circulation model simulations of the upper atmospheric response to a dust storm. They concluded that "the inflation of the entire Mars atmosphere due to aerosol heating dominates the overall change in density at a given altitude" and found that dust-induced changes to atmospheric circulation also play a role. Bougher et al. (1999) used coupled Mars General Circulation Model–Mars Thermosphere General Circulation Model (MGCM–MTGCM) simulations to study the Noachis dust storm and its effects on MGS atmospheric observations during aerobraking. They found that their simulations under-estimated the upper atmospheric effects of this dust storm and concluded that the root of the problem lay in their inability to fully integrate the circulation of the lower and upper regions of the atmosphere at the models' interface.

Subsequently, Bell et al. (2007) conducted a series of dynamical simulations of the atmosphere of Mars using an enhanced version of the coupled MGCM–MTGCM in which the atmospheric circulation was more fully integrated. They explored the effects of variations in vertical dust mixing in the lower atmosphere. They also explored the response to interannual variations in the spatial distribution of dust using MGS TES infrared dust opacity data from Mars Years 24 to 27.

Bell et al. (2007) conducted simulations at Ls = 90° in which the vertical extent of dust loading was increased from a Conrath parameter (ν) of 0.3–0.03, then 0.005 (dust mixing ratio drops to half its surface value at 1, 3, and 5 scale heights, respectively) whilst all other parameters, including total integrated dust opacity ($\tau = 0.3$), were held constant. They found that atmospheric number densities at 120 km increased from an equatorial zonal average value of 5.0×10^{10} cm^{-3} in the $\nu = 0.3$ simulation to 6.3×10^{10} cm^{-3} in the $\nu = 0.03$ simulation and 1.0×10^{11} cm^{-3} in the $\nu = 0.005$ simulation. At the winter pole, the increase is much greater, going from 2.0×10^{10} cm^{-3} to 5.0×10^{10} cm^{-3} and then 1.3×10^{11} cm^{-3}.

A 100% density increase at the equator is accompanied by a 650% density increase at the winter pole. The equatorial density increase simply "reflects the impacts of the lower atmosphere's inflation in response to increased lower atmospheric dust", while the amplified density increase at the winter pole "suggest[s] that the interhemispherical Hadley circulation dominating the neutral temperatures in the winter polar regions also appears to modify the winter polar thermosphere's neutral density structures significantly." There are five main processes that influence the structure of the upper atmosphere: thermal conduction, CO_2 15 μm cooling, solar heating, hydrodynamic advection, and adiabatic heating/cooling. Of these, Bell et al. (2007) found that adiabatic heating and cooling due to the convergence and divergence of atmospheric flows was the most important for influencing variations in the structure of the upper atmosphere due to variations in vertical dust distribution.

As dust was mixed higher into the atmosphere (decreasing Conrath parameter), the number density at 120 km increased. However, the number density at 180 km was affected much less. This suggests that the upper atmospheric effects of dust storms peter out at sufficiently high altitudes, consistent with the finding of Section 3.1 that the density enhancement factor appeared to decrease with increasing altitude from 130 km to 160 km.

Bell et al. (2007) also noted that upper atmospheric temperatures increased if the total integrated dust opacity increased or if the season was advanced to Ls = 270°, which is near perihelion, but did not quantify the associated density changes. However, they did conclude that the changes in atmospheric circulation, which lead to changes in adiabatic heating and cooling rates, were a major factor.

Surprisingly, Bell et al. (2007) did not find drastically different upper atmospheric conditions in the tropics at Ls = 270° in MY 25, when the atmosphere was recovering from a large dust storm and dust opacities remained above-average, relative to MYs 24 and 26, when dust opacities were more typical. Zonal mean equatorial number densities at 120 km were 1.0×10^{11} cm^{-3} in MY 24 and 25, but half that in MY 26. At many other latitudes, however, differences were apparent. At both poles, densities were larger in MY 25 than MY 24, and in MY 24 than MY 26, and southern hemispheric densities were greatest in MY 25. Despite significantly higher dust opacities in MY 25 than MY 26, equatorial densities were the same in the 2 years, which demonstrates that enhanced dust loading in the lower atmosphere is not by itself sufficient to impact the upper atmosphere.

The importance of whole atmosphere atmospheric circulation was effectively illustrated by Bell et al. (2007), who showed that diurnally averaging upward propagating effects at the MGCM–MTGCM interface (1.32 μbar, about 80 km) reduced the upper atmospheric winter polar warming and eliminating the lower atmosphere's contribution to upper atmospheric circulation eliminated the polar warming.

The numerical simulations demonstrate that inflation of the atmosphere in response to aerosol heating is only the first step by which the upper atmosphere is affected by dust storms. These temperature changes affect the interhemispheric Hadley circulation, whose strength, meridional extent, and vertical extent affect adiabatic heating and cooling at upper atmospheric altitudes. Changes to the circulation are the primary mechanism by which the effects of changes in lower atmospheric dust loading are transmitted to the upper atmosphere—they enable:

- A strong upper atmospheric response at latitudes far-removed from regions of enhanced dust loading (Section 4.2);
- heating at 70–120 km altitudes where the dust content is miniscule and cooling at 130–160 km altitudes where dust is not present (Section 4.3);

- a more rapid meridional advance of the onset of dust storm effects at upper atmospheric altitudes than the meridional advance of dust at lower altitude (Section 4.4);
- separation of decay timescales for changes in upper atmospheric conditions and changes in dust content (Section 4.5); and
- a very strong response in the winter polar regions.

Changes to the circulation are also responsible for the upper atmospheric response being characterized by large spatial scales, even when the dust event itself is more localized.

6. Conclusions

We confirm the conclusions of earlier studies that dust storms readily cause a sudden increase in upper atmospheric density, followed by a gradual decline to pre-storm conditions. The main findings of this work are:

(1) Upper atmospheric conditions can be perturbed by dust storms outside the classical "dust storm season" of Ls = 180–360°. THEMIS data show tropical dust events at Ls = 130–140° in MY 27, 28, and 29, whilst upper atmospheric data from this season in MY 27 show substantial density increases, suggesting that upper atmospheric disturbances that are caused by lower atmospheric dust events may routinely occur over most of the Mars Year, not merely half of it.

(2) The upper atmospheric regions affected by a dust event can include nearly all latitudes, which is consistent with previous numerical simulations of a vertically and horizontally extended dynamical response (with consequent heating and upwelling of pressure levels) to localized dust enhancements in the lower atmosphere.

(3) Atmospheric temperatures can be affected (heated or cooled) by dust storms at altitudes as high as 160 km, although dust is not lofted to those altitudes, which again demonstrates the importance of the large-scale dynamical response to localized dust enhancements in the lower atmosphere as the mechanism that drives changes in the upper atmosphere during dust storms.

(4) The onset of the upper atmospheric response to a distant dust event can be a few days or less. This, combined with the speed at which lower atmospheric dust content can rise at the start of a dust storm, presents a challenge for safe spacecraft operations at upper atmospheric altitudes.

(5) The characteristic timescale for the decay of the upper atmospheric response to a dust event can be 20–120° of Ls, and it may differ from the corresponding timescale for the lower atmosphere. The large range in decay timescales in the upper atmosphere and the apparent decoupling of upper and lower atmospheric decay timescales indicates interesting behavior in the response of the atmospheric circulation and thermal structure to dust storms; it is an issue ripe for exploration in numerical simulations. Larger density enhancements seem to decay more quickly than small ones.

(6) Average upper atmospheric densities can change by factors of a few during mere regional dust storms and an order of magnitude change is possible for the largest storms. These are general trends; individual density measurements may be greater than suggested by the general trend by a factor of two due to the intrinsic variability of the upper atmosphere. The most plausible interpretation of the observed variations in density enhancement factor with altitude is that it increases with altitude up to the mesopause, then decreases.

Acknowledgments

We acknowledge helpful reviews from Luca Montabone and an anonymous colleague, Luca Montabone again for providing easy access to THEMIS dust data, and partial support from the NASA Mars Data Analysis Program (NNX08AK96G) and Mars Critical Data Products Program (1407345).

References

Bell, J.M., Bougher, S.W., Murphy, J.R., 2007. Vertical dust mixing and the interannual variations in the Mars thermosphere. J. Geophys. Res. 112, E12002. http://dx.doi.org/10.1029/2006JE002856.

Bertaux, J.-L. et al., 2004. SPICAM: Studying the Global Structure and Composition of the Martian Atmosphere, pp. 95–120. ESA SP-1240: Mars Express: The Scientific Payload. <http://sci.esa.int/science-e/www/object/index.cfm?fobjectid=34885>.

Bertaux, J. et al., 2006. SPICAM on Mars Express: Observing modes and overview of UV spectrometer data and scientific results. J. Geophys. Res. 111, E10S90. http://dx.doi.org/10.1029/2006JE002690.

Böttger, H.M., Lewis, S.R., Read, P.L., Forget, F., 2004. The effect of a global dust storm on simulations of the martian water cycle. Geophys. Res. Lett. 31, L22702. http://dx.doi.org/10.1029/2004GL021137.

Bougher, S.W., Murphy, J., Haberle, R.M., 1997. Dust storm impacts on the Mars upper atmosphere. Adv. Space Res. 19, 1255–1260.

Bougher, S. et al., 1999. Mars Global Surveyor aerobraking: Atmospheric trends and model interpretation. Adv. Space Res. 23, 1887–1897.

Cantor, B.A., 2007. MOC observations of the 2001 Mars planet-encircling dust storm. Icarus 186, 60–96.

Cantor, B.A., James, P.B., Calvin, W.M., 2010. MARCI and MOC observations of the atmosphere and surface cap in the north polar region of Mars. Icarus 208, 61–81.

Christensen, P.R. et al., 1998. Results from the Mars Global Surveyor Thermal Emission Spectrometer. Science 279, 1692–1698.

Clancy, R.T., Wolff, M.J., Whitney, B.A., Cantor, B.A., Smith, M.D., McConnochie, T.H., 2010. Extension of atmospheric dust loading to high altitudes during the 2001 Mars dust storm: MGS TES limb observations. Icarus 207, 98–109.

Conrath, B.J., 1975. Thermal structure of the martian atmosphere during the dissipation of the dust storm of 1971. Icarus 24, 36–46.

Elteto, A., 2009. Martian Global Dust storm 2001A as Observed by the Mars Global Surveyor Thermal Emission Spectrometer. Ph.D. Thesis, University of Colorado at Boulder.

Elteto, A., Toon, O.B., 2010. The effects and characteristics of atmospheric dust during martian global dust storm 2001A. Icarus 210, 589–611.

Forget, F. et al., 2009. Density and temperatures of the upper martian atmosphere measured by stellar occultations with Mars Express SPICAM. J. Geophys. Res. 114, E01004. http://dx.doi.org/10.1029/2008JE003086.

Fritts, D.C., Wang, L., Tolson, R.H., 2006. Mean and gravity wave structures and variability in the Mars upper atmosphere inferred from Mars Global Surveyor and Mars Odyssey aerobraking densities. J. Geophys. Res. 111, A12304. http://dx.doi.org/10.1029/2006JA011897.

González-Galindo, F., Forget, F., López-Valverde, M.A., Angelats i Coll, M., 2009. A ground-to-exosphere martian general circulation model: 2. Atmosphere during solstice conditions – Thermospheric polar warming. J. Geophys. Res. 114, E08004. http://dx.doi.org/10.1029/2008JE003277.

Gurwell, M.A., Bergin, E.A., Melnick, G.J., Tolls, V., 2005. Mars surface and atmospheric temperature during the 2001 global dust storm. Icarus 175, 23–31.

Hantsch, M.H., Bauer, S.J., 1990. Solar control of the Mars ionosphere. Planet. Space Sci. 38, 539–542.

Heavens, N.G., McCleese, D.J., Richardson, M.I., Kass, D.M., Kleinböhl, A., Schofield, J.T., 2011a. Structure and dynamics of the martian lower and middle atmosphere as observed by the Mars Climate Sounder: 2. Implications of the thermal structure and aerosol distributions for the mean meridional circulation. J. Geophys. Res. 116, E01010. http://dx.doi.org/10.1029/2010JE003713.

Heavens, N.G. et al., 2011b. The vertical distribution of dust in the martian atmosphere during northern spring and summer: Observations by the Mars Climate Sounder and analysis of zonal average vertical dust profiles. J. Geophys. Res. 116, E04003. http://dx.doi.org/10.1029/2010JE003691.

Hinson, D.P., Wang, H., 2010. Further observations of regional dust storms and baroclinic eddies in the northern hemisphere of Mars. Icarus 206, 290–305.

Hinson, D.P., Simpson, R.A., Twicken, J.D., Tyler, G.L., Flasar, F.M., 1999. Initial results from radio occultation measurements with Mars Global Surveyor. J. Geophys. Res. 104, 26997–27012.

Keating, G.M. et al., 1998. The structure of the upper atmosphere of Mars: In situ accelerometer measurements from Mars Global Surveyor. Science 279, 1672–1676.

Kleinböhl, A. et al., 2009. Mars Climate Sounder limb profile retrieval of atmospheric temperature, pressure, and dust and water ice opacity. J. Geophys. Res. 114, E10006. http://dx.doi.org/10.1029/2009JE003358.

Kliore, A.J., Cain, D.L., Fjeldbo, G., Seidel, B.L., Sykes, M.J., Rasool, S.I., 1972. The atmosphere of Mars from Mariner 9 radio occultation measurements. Icarus 17, 484–516.

Kliore, A.J., Fjeldbo, G., Seidel, B.L., Sykes, M.J., Woiceshyn, P.M., 1973. S band radio occultation measurements of the atmosphere and topography of Mars with Mariner 9: Extended Mission coverage of polar and intermediate latitudes. J. Geophys. Res. 78, 4331–4351.

Lewis, S.R., Read, P.L., Conrath, B.J., Pearl, J.C., Smith, M.D., 2007. Assimilation of thermal emission spectrometer atmospheric data during the Mars Global Surveyor aerobraking period. Icarus 192, 327–347.

McDunn, T.L., Bougher, S.W., Murphy, J., Smith, M.D., Forget, F., Bertaux, J.-L., Montmessin, F., 2010. Simulating the density and thermal structure of the middle atmosphere (∼80–130 km) of Mars using the MGCM–MTGCM: A comparison with MEX/SPICAM observations. Icarus 206, 5–17.

McElroy, M.B., Kong, T.Y., Yung, Y.L., 1977. Photochemistry and evolution of Mars' atmosphere – A Viking perspective. J. Geophys. Res. 82, 4379–4388.

Mendillo, M., Withers, P., Hinson, D., Rishbeth, H., Reinisch, B., 2006. Effects of solar flares on the ionosphere of Mars. Science 311, 1135–1138.

Montabone, L., Lewis, S.R., Read, P.L., 2005. Interannual variability of martian dust storms in assimilation of several years of Mars Global Surveyor observations. Adv. Space Res. 36, 2146–2155.

Montabone, L., Lewis, S.R., Read, P.L., Withers, P., 2006. Reconstructing the weather on Mars at the time of the MERs and Beagle 2 landings. Geophys. Res. Lett. 33, L19202. http://dx.doi.org/10.1029/2006GL026565.

Pang, K., Hord, C.W., 1973. Mariner 9 ultraviolet spectrometer experiment: 1971 Mars dust storm. Icarus 18, 481–488.

Pätzold, M. et al., 2004. MaRS: Mars Express Orbiter Radio Science, pp. 141–163. ESA SP-1240: Mars Express: The Scientific Payload. <http://sci.esa.int/science-e/www/object/index.cfm?fobjectid=34885>.

Quémerais, E. et al., 2006. Stellar occultations observed by SPICAM on Mars Express. J. Geophys. Res. 111, E09S04. http://dx.doi.org/10.1029/2005JE002604.

Rafkin, S.C.R., 2009. A positive radiative-dynamic feedback mechanism for the maintenance and growth of martian dust storms. J. Geophys. Res. 114, E01009. http://dx.doi.org/10.1029/2008JE003217.

Smith, M.D., 2004. Interannual variability in TES atmospheric observations of Mars during 1999–2003. Icarus 167, 148–165.

Smith, M.D., 2008. Spacecraft observations of the martian atmosphere. Ann. Rev. Earth Planet. Sci. 36, 191–219.

Smith, M.D., 2009. THEMIS observations of Mars aerosol optical depth from 2002–2008. Icarus 202, 444–452.

Smith, M.D., Pearl, J.C., Conrath, B.J., Christensen, P.R., 2000. Mars Global Surveyor Thermal Emission Spectrometer (TES) observations of dust opacity during aerobraking and science phasing. J. Geophys. Res. 105, 9539–9552.

Smith, D.E. et al., 2001. Mars Orbiter Laser Altimeter: Experiment summary after the first year of global mapping of Mars. J. Geophys. Res. 106, 23689–23722.

Smith, M.D., Conrath, B.J., Pearl, J.C., Christensen, P.R., 2002. NOTE: Thermal Emission Spectrometer observations of martian planet-encircling dust storm 2001A. Icarus 157, 259–263.

Smith, M.D. et al., 2006. One martian year of atmospheric observations using MER Mini-TES. J. Geophys. Res. 111, E12S13. http://dx.doi.org/10.1029/2006JE002770.

Stewart, A.J., Hanson, W.B., 1982. Mars' upper atmosphere – Mean and variations. Adv. Space Res. 2, 87–101.

Tolson, R.H., Cancro, G.J., Keating, G.M., Noll, S.N., Parker, J.S., Wilkerson, B.L., 1999. Application of accelerometer data to Mars Global Surveyor aerobraking operations. J. Spacecraft Rockets 36, 323–329.

Tolson, R. et al., 2005. Application of accelerometer data to Mars Odyssey aerobraking and atmospheric modeling. J. Spacecraft Rockets 42, 435–443.

Tolson, R.H., Keating, G.M., Zurek, R.W., Bougher, S.W., Justus, C.G., Fritts, D.C., 2007. Application of accelerometer data to atmospheric modeling during Mars aerobraking operations. J. Spacecraft Rockets 44, 1172–1179.

Wang, J.-S., Nielsen, E., 2003. Behavior of the martian dayside electron density peak during global dust storms. Planet. Space Sci. 51, 329–338.

Withers, P., 2006. Mars Global Surveyor and Mars Odyssey Accelerometer observations of the martian upper atmosphere during aerobraking. Geophys. Res. Lett. 33, L02201. http://dx.doi.org/10.1029/2005GL024447.

Withers, P., 2009. A review of observed variability in the dayside ionosphere of Mars. Adv. Space Res. 44, 277–307.

Withers, P., Smith, M.D., 2006. Atmospheric entry profiles from the Mars Exploration Rovers Spirit and Opportunity. Icarus 185, 133–142.

Withers, P., Bougher, S.W., Keating, G.M., 2003. The effects of topographically-controlled thermal tides in the martian upper atmosphere as seen by the MGS accelerometer. Icarus 164, 14–32.

Withers, P., Mendillo, M., Hinson, D.P., Cahoy, K., 2008. Physical characteristics and occurrence rates of meteoric plasma layers detected in the martian ionosphere by the Mars Global Surveyor Radio Science Experiment. J. Geophys. Res. 113, A12314. http://dx.doi.org/10.1029/2008JA013636.

Withers, P., Pratt, R., Bertaux, J.-L., Montmessin, F., 2011. Observations of thermal tides in the middle atmosphere of Mars by the SPICAM instrument. J. Geophys. Res. 116, E11005. http://dx.doi.org/10.1029/2011JE003847.